Lab on a Chip

PAPER

View Article Online
View Journal | View Issue

Cite this: *Lab Chip*, 2015, **15**, 3147

Dielectrophoresis-assisted 3D nanoelectroporation for non-viral cell transfection in adoptive immunotherapy†

Lingqian Chang,‡[ab] Daniel Gallego-Perez,‡[b] Xi Zhao,[c] Paul Bertani,[d] Zhaogang Yang,[b] Chi-Ling Chiang,[b] Veysi Malkoc,[b] Junfeng Shi,[b] Chandan K. Sen,[e] Lynn Odonnell,[f] Jianhua Yu,[f] Wu Lu*[d] and L. James Lee*[abc]

Received 16th May 2015,
Accepted 17th June 2015

DOI: 10.1039/c5lc00553a

www.rsc.org/loc

Current transfection technologies lead to significant inter-clonal variations. Previously we introduced a unique electrotransfection technology, Nanochannel-Electroporation (NEP), which can precisely and benignly transfect small cell populations (~100–200 cells) with single-cell resolution. Here we report on the development of a novel 3D NEP system for large scale transfection. A properly-engineered array of nanochannels, capable of handling/transfecting ~60 000 cells cm^{-2}, was fabricated using cleanroom technologies. Positive dielectrophoresis was used to selectively position cells on the nanochannels, thus allowing highly efficient transfection. Single-cell dosage control was demonstrated using both small and large molecules, and different cell types. The potential clinical relevance of this system was tested with difficult-to-transfect natural killer cell suspensions, and plasmids encoding for the chimeric antigen receptor (CAR), a model of high relevance for adoptive immunotherapy. Our results show significantly higher CAR transfection efficiencies for the DEP-NEP system (>70% *vs.* <30%), as well as enhanced cell viabilities.

Introduction

A number of physical methods have been developed for gene transfection to cells in response to the limitations posed by viral vectors regarding safety concerns.[1–3] Among these, microinjection is the only approach that can provide cargo delivery directly into the cytosol, and with single-cell resolution. However, microinjection is labor-intensive and technically challenging, which limits its implementation to large-sized cells and small cell populations.[4–6] The Biolistic gene gun approach on the other hand involves propulsion-based delivery of DNA-coated beads into cells.[7] Such an approach is random in nature and usually results in irreversible damage to the cell membrane, thus considerably compromising cell viability. Electroporation, laser irradiation and sonoporation are alternative methods that can be used to reversibly disrupt the cell membrane and allow gene transfection.[8–10] Electroporation, in particular, offers a number of advantages over its competitors, and has been widely used both *in vitro* and *in vivo* in a variety of applications, including gene therapy, wound healing and drug screening.[11–14]

In bulk electroporation (BEP), a large cell population is confined within a pair of electrodes that are then used to apply high voltages to induce membrane poration and facilitate gene transfection.[15–17] A major drawback of BEP; however, is the fact that a significant proportion of cells are irreversibly damaged under such harsh conditions.[10,18] Moreover, there are substantial variations in the local electric field experienced by each cell, which results in random/stochastic gene transfection and expression.[18,19] A number of microfluidic-based electroporation (MEP) systems developed recently have been reported to minimize cell damage by reducing the distance between electrodes, thus facilitating electric field-induced poration at lower voltages.[17,18,20–22] Nevertheless, the process of cargo/gene uptake by the cells in both BEP and MEP is still heavily dependent upon diffusion and endocytosis, which poses a limitation for the internalization of bulky cargo, such as large (>7.5 kbp) plasmids, and it also makes it difficult to control the dosage, thus further contributing to the stochastic nature of these approaches.[23]

[a] *Department of Biomedical Engineering, The Ohio State University, Columbus, Ohio 43210, USA. E-mail: lee.31@osu.edu*
[b] *Nanoscale Science and Engineering Center for Affordable Nanoengineering of Polymeric Biomedical Devices, The Ohio State University, Columbus, Ohio 43210, USA*
[c] *Department of Chemical and Biomolecular Engineering, The Ohio State University, Columbus, Ohio 43210, USA*
[d] *Department of Electrical and Computer Engineering, The Ohio State University, Columbus, Ohio 43210, USA. E-mail: lu.173@osu.edu*
[e] *Department of Surgery, The Ohio State University, Columbus, Ohio 43210, USA*
[f] *Department of Internal Medicine, The Ohio State University, Columbus, OH 43209, USA*
† Electronic supplementary information (ESI) available. See DOI: 10.1039/c5lc00553a
‡ Equal contribution.

Being able to deliver well-defined amounts of cargo (*e.g.*, plasmids, small oligonucleotides, *etc.*) into cells could be of high significance for many biological and medical applications. Recently we developed a novel and unique nanochannel electroporation (NEP) technology where cargo delivery is achieved by a focused electric field through a nanochannel juxtaposed to a single cell.[24,25] The field nanoporates the cell, and provides electrophoretic motility to directly deliver charged cargo into the cytosol in a controlled and benign manner. The nanochannel also serves as a diffusion barrier to prevent any further/unwanted cargo delivery after poration. The voltage, pulse length and number of pulses can be readily adjusted to precisely control the amount of cargo delivered at the single-cell level. This system; however, was based on a two-dimensional (2D) design that had a relatively limited throughput (*i.e.*, single to ~200 cells).

Herein we report the development of a three-dimensional (3D) NEP system for benign and controlled single-cell electrotransfection of large cell populations. Unlike other systems, where commercially-available nanoporous track-etched membranes were used to arbitrarily transfect cultured cells through a highly dense and random array of nanochannels,[26–28] and in which the cells are highly susceptible to joule heating during poration due to the low electrical resistivity across the membrane; the device developed herein is comprised of a properly-engineered/ordered array of silicon (Si) nanochannels that can be precisely interfaced with single cells *via* positive dielectrophoresis (pDEP), thereby allowing for controlled cargo delivery with single cell resolution and negligible cell damage, even at the relatively high voltages (>100 V) required for successful transfection of large plasmids. The dosage control capabilities of such system were demonstrated using both small and large cargo (*e.g.*, propidium iodide (PI), fluorescently-labeled oligos, 3.5–9 kbp plasmids). Finally, the potential clinical significance of the 3D NEP platform was tested using a model of relevance to adoptive immunotherapy, where natural killer (NK) cells were efficiently transfected with a plasmid encoding for the chimeric antigen receptor (CAR), which presumably enhances antitumor activity in NK cells.[29,30]

Experimental

Wafer-scale fabrication of 3D NEP platform

The platform was fabricated based on a combination of projection, contact photolithography, and deep reactive ion-etch (DRIE). A 500 μm thick double-side polished silicon wafer (100) was first thinned down to 250 μm *via* wet etching in a 45% KOH solution at 80 °C (approximate etch rate ~1 μm min^{-1}). A ~600 nm thick layer of SPR-950 was then spin coated on one side of the wafer. Arrays of nanochannels were subsequently patterned through the photoresist using projection photolithography (GCA 6100C Stepper), which was then followed by 40 cycles (~10 μm depth) of DRIE (Oxford Plasma Lab 100 system). For this we used a Bosch process with optimized parameters (SF6 gas: 13 s/100 sccm gas flow/700 W ICP power/40 W RF power/30 mT APC pressure; C4F8 gas condition: 7 s/100 sccm gas flow/700 W ICP power/10 W RF power/30 mT APC pressure). Once the nanochannel arrays were defined on the Si surface, the wafer was flipped over to pattern an array of microreservoirs *via* contact photolithography using SPR220-7. This was then followed by ~250 cycles (~240 μm depth) of DRIE to expose the ends of the nanochannels. Finally, the nanochannel side of the platform was coated with an insulating Si_3N_4 layer *via* plasma-enhanced chemical vapor deposition.

Finite element analysis

Simulation studies were conducted in Comsol Multiphysics (COMSOL, MA). For DEP, a model was developed based on the geometry of the 3D NEP system and the electrical properties of a cell, which was modeled by a 15 μm diameter sphere. The 5 nm thick cell membrane was considered as a surface impedance layer to avoid mesh density overflow. The conductivity of the isotonic sucrose solution was measured to be ~0.03 S m^{-1}. A potential drop of 50 V was assigned across two planes on opposite sides of nanochannel, both of which were 50 μm away from the silicon surface. Simulations for electrical continuity were conducted at 500 Hz and 100 kHz to generate current density distributions during negative and positive DEP, respectively.

3D DEP-NEP platform assembly

The PDMS stencils were made from a pre-polymer/curing agent mixture (Sylgard 184, Dow Corning) at a 10 : 1 ratio. The PDMS was allowed to cure at room temperature for ~48 h prior to assembling the platform. The PDMS surface was pre-treated with oxygen plasma (PTS oxygen plasma system) to secure the stencil to the platform. The bottom electrode was prepared by e-beam evaporation (Denton DV-502A) of Au on a glass substrate. An ITO-coated glass was used as the top electrode. An upright microscope (Leica Microsystems DM2500 MH) was used for real-time monitoring of the cells during NEP, and an inverted microscope (Nikon Eclipse Ti) was used to visualize the cells after NEP-based electroinjection.

Dielectrophoresis

A custom-built power supply was used to generate a differential AC signal with a maximum peak-to-peak voltage (V_{pp}) of 100 V. The DEP driver consisted of a signal generator and an amplifier. Symmetric square waves (~0.8 V_{pp}) from a digital function generator (DS345, Stanford Research Systems) were fed into the amplifier. A LM6172 operational amplifier (Texas Instruments) was used to enhance the signal. To maximize ∇E^2 on the NEP device, the operational amplifiers in the circuit were configured for open loop operation, and a square wave feed was selected over other functions, both of which helped minimize the slew rate of the circuit. The output amplitude was controlled by the voltage supplied to the

LM6172. Although the maximum supply voltage of the LM6172 was 36 V, stable operation at 54 V was achieved with the addition of heat sink. The circuit yields both in-phase and reversed-phase outputs, which were used as the differential driving signal for DEP to produce a stronger field. An oscilloscope with differential probes (Tektronix TDS 3034C) was used to monitor and record signals from both the DEP and NEP power supplies during the experiments. DEP/NEP switching was conducted *via* manual operation of a set of microswitches on the circuit.

Bulk electroporation

A commercial BEP system (Neon Transfection System, Life Technologies) was used for comparison purposes. Specific electric field conditions were implemented following the suppliers' instructions, depending on the cell type.

Cells experiments

H9C2 and NK-92 cells were purchased from ATCC. H9C2 cells were cultured in Dulbecco's Modified Eagle's Medium (Catalog no. 30-2002, Life Technologies) with 10% fetal bovine serum (Catalog no. 16000-044, Life Technologies). NK-92 cells on the other hand were maintained in RPMI 1640 with 20% FBS and a 1 : 1000 dilution of IL-2 (Catalog no. 12633-012, Life Technologies). Calcein AM (Catalog no. L3224A, Life Technologies) was used to identify live cells following pDEP-NEP. Fluorescently-labeled oligodeoxynucleotides (ODN) were purchased from Alpha DNA (Catalog no. 427520). Propidium iodide (PI) was purchased from Invitrogen (Cat. no. P3566). The pmaxGFP plasmid (Catalog no. VSC-1001) was obtained from Amaxa Nucleofector Technology. Additional information on the CAR plasmid can be found elsewhere.[31]

Statistical analysis

A two-sided student *t*-test was used to determine the significance for data with normal distribution and equal variances. All other data were analyzed using either the Dunn's or Tukey method.

Results and discussion

Fabrication and assembly of the 3D NEP platform

A wafer-scale process (Fig. 1) was developed for the fabrication of well-defined arrays of Si nanochannels (~300–650 nm cross-section with a 50 μm pitch). Briefly, a combination of

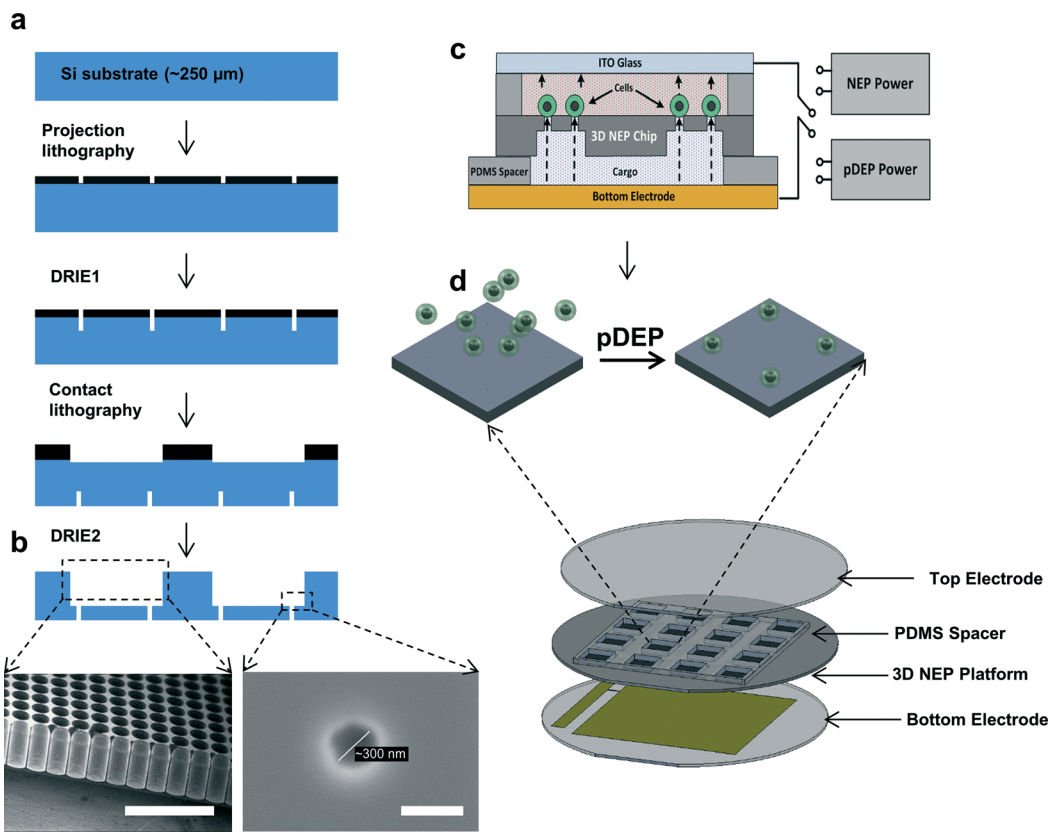

Fig. 1 Fabrication and assembly of a 3D DEP-NEP system for large scale single-cell transfection. (a) Fabrication schematic of the nanochannel array. (b) Scanning electron micrographs of the nanochannels and microreservoirs. Scale bars (from left to right) = 500 μm and 500 nm. (c, d) Schematic diagram of the 3D DEP-NEP platform. A wafer-scale fabrication process was developed in order to handle up to 10^6 cells per platform. pDEP was used to precisely position cells in close proximity to the nanochannel outputs. The platform is comprised of a 4 × 4 array of nanoporating zones (~1–1.5 cm^2) on a single wafer. With a density of ~40 000–60 000 nanochannels per zone, each wafer has the capability to NEP-transfect ~0.6–1 million cells.

stepper projection lithography and deep reactive ion etching (DRIE) was first used to drill sixteen ~1 cm^2 arrays of nanochannels (10 μm deep) on a 250 μm thick double-side polished 10 cm (4 inch) Si wafer (Fig. 1a). The back-side of the wafer was subsequently photolithographically-patterned and DRI-etched (~240 μm) with an array of microwells (Fig. 1b) to expose the nanochannel ends and provide microscale reservoirs that could hold the cargo to be NEP-delivered into the cells. Fig. 1b shows scanning electron micrographs of both the nanochannel and the microwell cargo reservoirs.

The 3D NEP platform was subsequently assembled by compartmentalizing each array of nanochannels with a ~2 mm thick polydimethylsiloxane (PDMS) stencil on both sides, as well as interfacing with the proper electrode system required for applying the nanoporating and DEP electric fields (Fig. 1c and d). An e-beam gold-coated and an ITO-coated glass substrate/wafer were used as bottom and top electrodes, respectively. The semitransparent ITO electrode allowed for monitoring/imaging of the cells in real time using an upright microscope. The cell suspension was pre-loaded directly on top of the nanochannel array, while the solution containing the cargo (*e.g.*, plasmids, PI dye, labeled DNA) to be delivered was loaded on the opposite side, both within the confines of the PDMS reservoir (Fig. 1d). Positive or negative electric fields were then applied across the nanochannel array depending on the charge nature of the cargo.

Operation of the 3D DEP-NEP platform

Since the porating electric field is focused inside the nanochannel, and drops substantially outside of it, successful single-cell NEP-based transfection is highly dependent upon tight contact between the cell membrane and the nanochannel.[24] The magnitude of both the porating electric field and the transmembrane potential quickly decay as the cell moves away from the nanochannel outlet. This is even more critical when trying to transfect suspension cells, as these cells are more susceptible to drift away under convection and Brownian motion. Positive dielectrophoresis (pDEP) was then implemented to position and hold individual cells tightly on the nanochannel outlets.[22,32] The pDEP conditions involved a 50 V (V_{pp} = 100 V) alternating current (AC) square wave at 100 kHz (Fig. 2a). Such conditions were deemed optimum for precise and efficient co-localization of the cells with the nanochannels.

The direction of the DEP force with respect to the electric field gradient was determined by the Clausius–Mossotti function.[33] Positive (pDEP) or negative (nDEP) dielectrophoresis indicated whether any given cell would move towards or away from the regions of a higher electric field (*i.e.*, nanochannel), respectively (Fig. 2a). Simulation results suggested that under physiological buffer conditions, the cells will always undergo nDEP regardless of the used frequency. However, a low conductivity buffer in combination with high frequencies could allow the cells to experience pDEP towards the nanochannel outlets (see Fig. S1 in ESI†). We used low conductivity (0.03 S m^{-1}) isotonic solutions to run our DEP-NEP experiments. Under such conditions, the current density distribution as well as the orientation of the dielectrophoretic forces (*e.g.*, nDEP *vs.* pDEP) could change significantly within the 0.5–100 kHz frequency range, with lower frequencies resulting in nDEP while higher frequencies promoted pDEP (Video S1†).

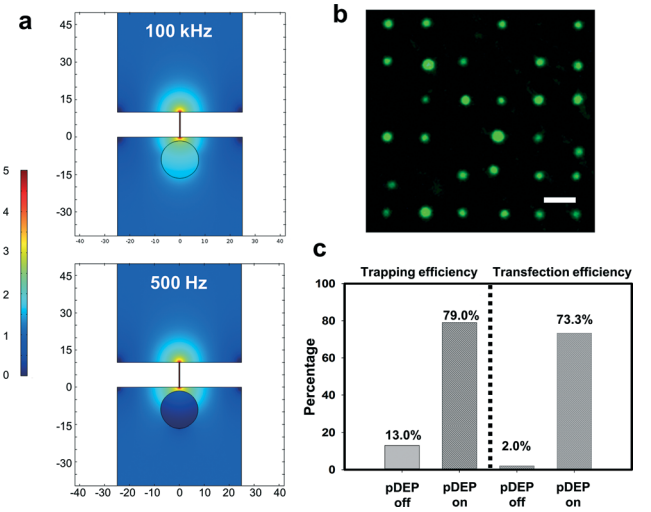

Fig. 2 pDEP can be used to precisely position cells on the nanochannel outputs. (a) Current density distribution in 3D NEP device under different DEP frequencies. (b) NK-92 cells (stained with Calcein AM) precisely located on the nanochannel outputs. Scale bar = 50 μm. (c) Quantification of cell trapping and transfection efficiencies on the 3D DEP-NEP platform.

Overall, the operation of the 3D DEP- NEP platform for high-throughput cell transfection involved the following steps: (1) cells were resuspended in low conductivity isotonic buffer and loaded on the chip surface; (2) pDEP was then applied across the top and bottom electrodes in order to position single cells on the nanochannel outlets; (3) pDEP was switched off and DC square wave pulses were immediately applied across the electrodes to nanoelectroporate the cells; (4) the low conductivity isotonic buffer was finally replaced by regular cell culture medium. Cell densities in step 1 were maintained within the range of the nanochannel array density.

A proof-of-concept experiment was then devised using a difficult to transfect NK suspension cell line (NK-92)[34,35] to test the performance of the 3D DEP-NEP set-up. About 79% of the cells were successfully placed on the nanochannels following pDEP implementation (Fig. 2b). Random loading of cells on the 3D NEP device, on the other hand, only resulted in a ~13% nanochannel occupancy rate. A direct current (DC) square wave pulse was subsequently implemented to NEP-transfect fluorescently-labeled ODN into the cells. Since ODN has a net negative charge, the top ITO electrode was positively charged, while the bottom gold electrode was negatively charged. Our results indicated that ~73% of the loaded cells (*i.e.* ~93% of the cells on the nanochannels) were successfully transfected under DEP-NEP, compared to only ~2% for random cell loading. Live/dead cell staining with Calcein AM

further confirmed that the pDEP and low conductivity buffer conditions did not negatively affect cell viability (Fig. 2c).

Functional voltage range and dosage control

We also probed a wide voltage range to determine the operational window for successful 3D DEP-NEP implementation. An adherent H9C2 cell line was used to conduct these experiments. Fluorescently-labeled ODN was again used as a model cargo. The cells on the platform were exposed to a DC square wave pulse (5 pulses, 10 ms duration, 1 s interval) with different voltages through the nanochannels. The transfection extent was estimated based on the amount of fluorescence emitted by single cells after ODN delivery. Fig. 3a shows that the implementation of low voltages (<15 V) did not result in significant/detectable accumulation of labeled ODN molecules in the cytosol compared to cells that were NEP-treated with PBS alone (p = 0.18). Higher voltages were required in order to achieve significant cytosolic accumulation of ODN ($p < 0.005$). Our results show that at relatively low applied voltages (<15 V), the transmembrane potential is not likely to be high enough to lead to a significant amount cell poration and cargo translocation. In contrast, higher voltages presumably resulted in enhanced degrees of poration and subsequent transfection, which appeared to be proportional to the voltage magnitude up to a certain value (~100 V). Beyond this point; however, increased voltages did not necessarily result in enhanced ODN accumulation, which could potentially be due to the saturation of the fluorescence signal and/or ODN uptake in a single cell.

A hallmark of the 3D DEP-NEP system is the ability to control the amount of delivered cargo to any large cell populations at the single cell level. This was demonstrated by NEP-delivering of fluorescence-labeled ODN to H9C2 cells under different conditions (Fig. 3b). A single square-wave pulse (140 V) with varying durations was applied across the electrodes of the 3D DEP-NEP platform. The results indicate that increasing the pulse duration leads to proportionally-enhanced ODN delivery into the cytosol with little cell-to-cell variations, as evidenced by the small error bars.

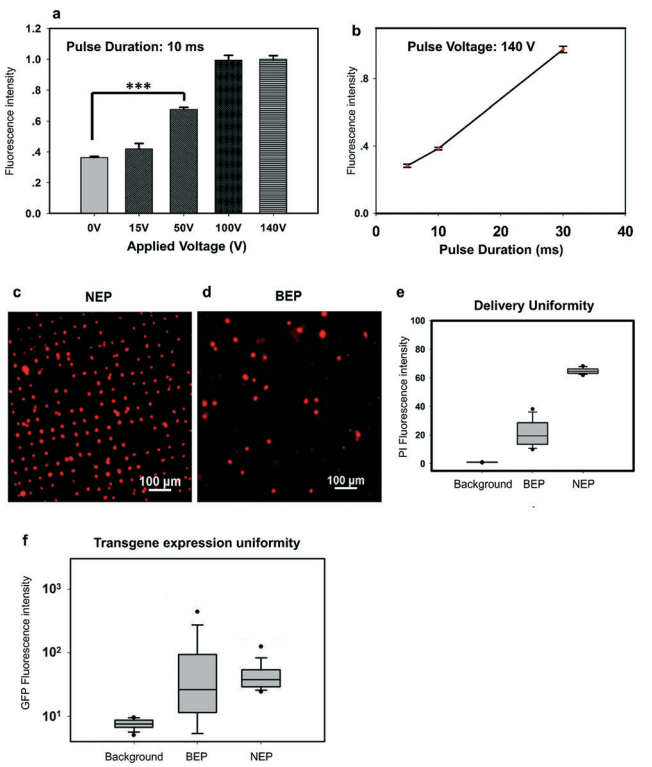

Fig. 3 3D NEP leads to stronger and more uniform delivery and transgene expression. Single-cell (H9C2) fluorescence intensity values for (a) different applied voltages (***$p < 0.005$, t-test) and (b) pulse durations. Fluorescence micrographs of H9C2 cells after (c) NEP- and (d) BEP-based delivery of PI dye. (e) Single-cell fluorescence intensity measurements after PI injection showing significantly more uniform delivery patterns for NEP compared to BEP. (f) Single-cell transgene expression extent for pmax-GFP plasmids.

Homogeneous NEP electroinjection and transgene expression

To further test the ability of the 3D DEP-NEP setup to uniformly deliver cargo to a large cell population we used PI dye, a positively-charged molecule that binds to DNA, as a model cargo. H9C2 cells on the platform were NEP-treated with square wave pulses (140 V, 10 ms). In this case the top ITO electrode and counter electrode were negatively- and positively-charged, respectively. Control experiments were conducted with a widely used Neon® Transfection BEP System (Life technologies).

Although both NEP and BEP successfully delivered PI dye into the cells, as evidenced by the emitted fluorescence once the dye reacted with intracellular nucleic acids (Fig. 3c–e), NEP-treated cells showed significantly stronger intensity compared to the BEP group ($p < 0.005$). Fig. 3c shows a large scale cell array on the 3D platform after NEP-based delivery of PI dye. Here, PI fluorescence could be detected in the cells right after pulse implementation (≪1 min), thus suggesting that delivery occurred by direct injection into the cytosol during poration. In the case of BEP (Fig. 3d); however, the fluorescence signal could only be detected several minutes after the exposure to the electric field, which again indicates that cargo delivery in BEP is heavily dependent upon a slower diffusion-based process. Moreover, while huge variations in the fluorescence intensity could be detected for the BEP group at the single cell level, the NEP-treated cells showed a very uniform delivery distribution (Fig. 3e), with single-cell fluorescence intensities that deviated only <1% from the mean value, compared to a ~50% variation for BEP.

Additional experiments were conducted to test whether uniform cargo delivery could also translate into more predictable cargo activity. In the case of plasmids/genes, gene expression is regulated downstream of delivery by intrinsic cellular sub-processes that are difficult to control. As such, stochastic delivery, which is typical in most transfection technologies, including BEP and viruses, is likely to result in less predictable gene activity, which could be problematic for

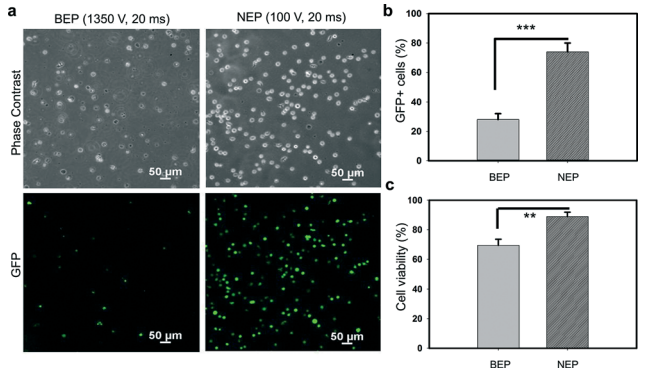

Fig. 4 Efficient non-viral NK-cell engineering by 3D DEP-NEP. (a) Fluorescence and phase contrast micrographs of NK cells 10 h after BEP- and NEP-based transfection of CAR plasmids. Positive fluorescence of the reporter gene (GFP) indicates successful expression of the target gene (CAR). NEP-based transfection resulted in (b) more efficient plasmid delivery and expression (***$p < 0.005$, *t*-test). NEP also promoted (c) improved cell viability compared to BEP (**$p < 0.01$, *t*-test).

many biomedical applications such as cell reprogramming and gene therapy. We hypothesized that controlled NEP-based delivery of plasmids/genes could lead to more uniform single-cell transgene expression levels. Our results indeed indicate that 3D NEP-based delivery of plasmids (*i.e.*, pmaxGFP) into H9C2 cells led to significantly stronger and considerably more homogeneous plasmid expression patterns compared to BEP (Fig. 3f).

Controlled and efficient non-viral NK-cell engineering by 3D DEP-NEP

Designer immune cells (*e.g.*, T cells, NK cells) are transgenically-engineered so as to be used in a number of applications, including enhancing antitumor immunity, improving vaccine efficacy, and reducing the incidence of graft-*versus*-host-disease. Adoptive cancer immunotherapy, in particular, could involve the re-targeting of NK cells to a given tumor antigen *via* transgenesis of an antigen-specific receptor, such as the chimeric antigen receptor (CAR).[29,35–38] Immune cell engineering; however, is still heavily dependent on viral methods, which could potentially hamper successful implementation due to safety concerns.[39] On the other hand, T and NK cells are notoriously difficult to transfect,[40] and thus non-viral methods have so far fell short in terms of transfection yields.

Here we tested whether our novel pDEP-assisted 3D NEP system could be used to efficiently and controllably transfect NK cells with plasmids encoding for CAR.[31] BEP (Neon®)-based transfection was again used for comparison purposes. NK-92 (ATCC) cells were loaded on the 3D DEP-NEP device and subsequently transfected using a single square wave pulse with 100 V amplitude and a 20 ms duration. A specific transfection protocol for immune cells was followed for BEP-based transfection (single 1350 V pulse with a 20 ms duration). CAR plasmid expression was then characterized in terms of GFP reporter gene activity 10 h after transfection *via* fluorescence imaging. We found that 3D DEP-NEP resulted in significantly higher transfection yields compared to BEP (74% *vs.* 28%, $p < 0.005$) (Fig. 4a and b), as well as a higher single-clone CAR expression extent ($p < 0.001$, Tukey Test), with average single cell GFP intensities of 9205 ± 2989 (average ± standard deviation) RFUs for NEP, and 2959 ± 1774 RFUs for BEP, thus suggesting that NEP-based transfection led to more uniformly-engineered and presumably safer cells, which could be of high relevance for clinical applications. BEP-based transfection also led to a marked decrease in cell viability compared to NEP (Fig. 4c), as determined by PI dye staining.

Conclusions

A novel nanotechnology-based approach was introduced here for safe, consistent and efficient transfection of large cell populations with single-clone resolution, a feature not achievable by any of the existing transfection technologies. A simple cleanroom-based protocol was developed to fabricate massively-parallel ordered arrays of nanochannels that could be used to transfect, in combination with positive dielectrophoresis (pDEP)- based cell manipulation, tens of thousands to hundreds of thousands of single cells in a fast, efficient, benign and controlled manner. High transfection yields, dosage control capabilities, as well as transfection and transgene expression uniformities were successfully demonstrated using different cell and cargo models, thus demonstrating the versatility of the 3D DEP-NEP platform. Such innovative nanotechnology could find use in many biomedical applications ranging from cell reprogramming to gene therapy among others.

Author contributions

L. C. and D. G. P. contributed equally to this work. L. C., D. G. P., W. L., L. J. L. wrote this manuscript. L. C., D. G. P. and P. B. carried out the 3D NEP platform fabrication. W. L. supervised the NEP device fabrication efforts. X. Z., L. C., D. G. P. and L. J. L conceived/developed 3D DEP-NEP system. L. C., D. G. P., V. M. and J. S. conducted NEP experiments. L. C., D. G. P., Z. Y. and C. C. analyzed the transfection data. J. Y., L. O., and C. K. S provided key support for the NK cell experiments in terms of resources, experimental design, data analysis/interpretation, and helpful discussion.

References

1 S. Mehier-Humbert and R. H. Guy, *Adv. Drug Delivery Rev.*, 2005, **57**, 733–753.
2 M. Costa, M. Dottori, K. Sourris, P. Jamshidi, T. Hatzistavrou, R. Davis, L. Azzola, S. Jackson, S. M. Lim, M. Pera, A. G. Elefanty and E. G. Stanley, *Nat. Protoc.*, 2007, **2**, 792–796.
3 K. Kaji, K. Norrby, A. Paca, M. Mileikovsky, P. Mohseni and K. Woltjen, *Nature*, 2009, **458**, 771–775.

4 H. Chantrenne, *Nature*, 1977, **269**, 202–202.
5 Z. Ivics, L. Hiripi, O. I. Hoffmann, L. Mates, T. Y. Yau, S. Bashir, V. Zidek, V. Landa, A. Geurts, M. Pravenec, T. Rulicke, Z. Bosze and Z. Izsvak, *Nat. Protoc.*, 2014, **9**, 794–809.
6 M. J. Layden, E. Rottinger, F. S. Wolenski, T. D. Gilmore and M. Q. Martindale, *Nat. Protoc.*, 2013, **8**, 924–934.
7 M. Zernicka-Goetz, *Nature*, 2000, **405**, 733–733.
8 U. K. Tirlapur and K. Konig, *Nature*, 2002, **418**, 290–291.
9 P. Chakravarty, W. Qian, M. A. El-Sayed and M. R. Prausnitz, *Nat. Nanotechnol.*, 2010, **5**, 607–611.
10 Y. C. Wu, T. H. Wu, D. L. Clemens, B. Y. Lee, X. Wen, M. A. Horwitz, M. A. Teitell and P. Y. Chiou, *Nat. Methods*, 2015, **12**, 439–444.
11 M. R. Prausnitz, V. G. Bose, R. Langer and J. C. Weaver, *Proc. Natl. Acad. Sci. U. S. A.*, 1993, **90**, 10504–10508.
12 C. M. Barbon, L. Baker, C. Lajoie, U. Ramstedt, M. L. Hedley and T. M. Luby, *Vaccine*, 2010, **28**, 7852–7864.
13 E. L. Ayuni, A. Gazdhar, M. N. Giraud, A. Kadner, M. Gugger, M. Cecchini, T. Caus, T. P. Carrel, R. A. Schmid and H. T. Tevaearai, *PLoS One*, 2010, 5.
14 T. Geng and C. Lu, *Lab Chip*, 2013, **13**, 3803–3821.
15 S. Y. Ho and G. S. Mittal, *Crit. Rev. Biotechnol.*, 1996, **16**, 349–362.
16 E. G. Guignet and T. Meyer, *Nat. Methods*, 2008, **5**, 393–395.
17 Y. C. Xu, Y. Lu and W. L. Xing, *Lab Chip*, 2014, **14**, 686–690.
18 W. Kang, J. P. Giraldo-Vela, S. S. P. Nathamgari, T. McGuire, R. L. McNaughton, J. A. Kessler and H. D. Espinosa, *Lab Chip*, 2014, **14**, 4486–4495.
19 M. dal Maschio, D. Ghezzi, G. Bony, A. Alabastri, G. Deidda, M. Brondi, S. S. Sato, R. P. Zaccaria, E. Di Fabrizio, G. M. Ratto and L. Cancedda, *Nat. Commun.*, 2012, 3.
20 M. Khine, A. Lau, C. Ionescu-Zanetti, J. Seo and L. P. Lee, *Lab Chip*, 2005, **5**, 38–43.
21 J. El-Ali, P. K. Sorger and K. F. Jensen, *Nature*, 2006, **442**, 403–411.
22 T. Geng, Y. Zhan, J. Wang and C. Lu, *Nat. Protoc.*, 2011, **6**, 1192–1208.
23 L. Q. Chang, M. Howdyshell, W. C. Liao, C. L. Chiang, D. Gallego-Perez, Z. G. Yang, W. Lu, J. C. Byrd, N. Muthusamy, L. J. Lee and R. Sooryakumar, *Small*, 2015, **11**, 1818–1828.
24 P. E. Boukany, A. Morss, W. C. Liao, B. Henslee, H. C. Jung, X. L. Zhang, B. Yu, X. M. Wang, Y. Wu, L. Li, K. L. Gao, X. Hu, X. Zhao, O. Hemminger, W. Lu, G. P. Lafyatis and L. J. Lee, *Nat. Nanotechnol.*, 2011, **6**, 747–754.
25 K. L. Gao, L. Li, L. N. He, K. Hinkle, Y. Wu, J. Y. Ma, L. Q. Chang, X. Zhao, D. G. Perez, S. Eckardt, J. Mclaughlin, B. Y. Liu, D. F. Farson and L. J. Lee, *Small*, 2014, **10**, 1015–1023.
26 X. Xie, A. M. Xu, S. Leal-Ortiz, Y. H. Cao, C. C. Garner and N. A. Melosh, *ACS Nano*, 2013, **7**, 4351–4358.
27 C. Xie, Z. L. Lin, L. Hanson, Y. Cui and B. X. Cui, *Nat. Nanotechnol.*, 2012, **7**, 185–190.
28 Z. Z. Fei, X. Hu, H. W. Choi, S. N. Wang, D. Farson and L. J. Lee, *Anal. Chem.*, 2010, **82**, 353–358.
29 S. A. Grupp, M. Kalos, D. Barrett, R. Aplenc, D. L. Porter, S. R. Rheingold, D. T. Teachey, A. Chew, B. Hauck, J. F. Wright, M. C. Milone, B. L. Levine and C. H. June, *N. Engl. J. Med.*, 2013, **368**, 1509–1518.
30 J. N. Kochenderfer and S. A. Rosenberg, *N. Engl. J. Med.*, 2011, **365**, 1937–1938; author reply 1938.
31 J. Chu, Y. Deng, D. M. Benson, S. He, T. Hughes, J. Zhang, Y. Peng, H. Mao, L. Yi, K. Ghoshal, X. He, S. M. Devine, X. Zhang, M. A. Caligiuri, C. C. Hofmeister and J. Yu, *Leukemia*, 2014, **28**, 917–927.
32 C. T. Ho, R. Z. Lin, W. Y. Chang, H. Y. Chang and C. H. Liu, *Lab Chip*, 2006, **6**, 724–734.
33 M. Urdaneta and E. Smela, *Lab Chip*, 2008, **8**, 550–556.
34 J. H. Gong, G. Maki and H. G. Klingemann, *Leukemia*, 1994, **8**, 652–658.
35 S. S. Somanchi, C. J. Denman, A. Amritkar, V. Senyukov, S. Olivares, L. J. N. Cooper and D. A. Lee, *Blood*, 2009, **114**, 973–973.
36 D. L. Porter, B. L. Levine, M. Kalos, A. Bagg and C. H. June, *N. Engl. J. Med.*, 2011, **365**, 725–733.
37 C. Krug, B. Saenger, M. Chmielewski, K. Birkholz, M. Schwenkert, G. Fey, G. Schuler, H. Abken, J. Dorrie and N. Schaft, *Exp. Dermatol.*, 2014, **23**, E25–E26.
38 C. C. Yeh, *N. Engl. J. Med.*, 2011, **365**, 1937, author reply 1938.
39 H. Buning, W. Uckert, K. Cichutek, R. E. Hawkins and H. Abken, *Hum. Gene Ther.*, 2010, **21**, 1039–1042.
40 Y. Zhao, E. Moon, C. Carpenito, C. M. Paulos, X. Liu, A. L. Brennan, A. Chew, R. G. Carroll, J. Scholler, B. L. Levine, S. M. Albelda and C. H. June, *Cancer Res.*, 2010, **70**, 9053–9061.